RESEARCH ARTICLE

Polarized Raman spectroscopy on topological semimetal $Co_3Sn_2S_2$

Kenya Tanaka[1] | **Taishi Nishihara**[1] | **Akira Takakura**[1] |
Yasutomo Segawa[2,3] | **Kazunari Matsuda**[1] | **Yuhei Miyauchi**[1]

[1]Institute of Advanced Energy, Kyoto University, Uji, Japan

[2]Institute for Molecular Science, Okazaki, Japan

[3]Department of Structural Molecular Science, SOKENDAI (The Graduate University for Advanced Studies), Okazaki, Japan

Correspondence
Yuhei Miyauchi, Institute of Advanced Energy, Kyoto University, Uji 611-0011, Japan.
Email: miyauchi@iae.kyoto-u.ac.jp

Funding information
JSPS KAKENHI, Grant/Award Numbers: JP20H02605, JP20H05664, JP21J15167, JP21H05232, JP21H05235, JP22K18986; JST CREST, Grant/Award Numbers: JPMJCR16F3, JPMJCR18I5; Future Development Funding Program of Kyoto University Research Coordination Alliance

Abstract

We present polarized Raman spectroscopy of the topological semimetal $Co_3Sn_2S_2$, which was recently shown to host a Weyl semimetal phase. Stokes Raman spectra were obtained with the incident light parallel to the c-axis of $Co_3Sn_2S_2$. Two major phonon Raman peaks were observed at 289 and 386 cm^{-1} over continuous background emission signals. The intensity of the low-wavenumber (289 cm^{-1}) peak showed no polarization dependence. The high-wavenumber (386 cm^{-1}) peak and the continuous background signal were strongly polarized in the incident light polarization direction. These responses were almost independent of the in-plane crystal orientation to the incident polarization, as is the manifestation of the D_{3d} point group symmetry of the unit cell of $Co_3Sn_2S_2$. According to the group theory and Raman tensor analyses, the low- and high-wavenumber Raman signals are attributed to Γ point phonon modes with E_g and A_{1g} symmetries, respectively. Furthermore, line shape analyses revealed that the high-wavenumber A_{1g} mode exhibited asymmetric peak feature well described by the Breit–Wigner–Fano function. These results suggest the Fano resonance between the A_{1g} phonon scattering with the continuous electronic background associated with low energy excitations near the Fermi energy. The clarified phonon energies and symmetries, as well as the electronic contribution to the Raman scattering, will not only be useful as a fingerprint to readily verify the experimentally grown or theoretically calculated crystal structure but also suggest importance of Raman spectroscopy as an effective tool to study low energy excitations and their interactions in $Co_3Sn_2S_2$.

KEYWORDS
electronic Raman scattering, phonon, polarized Raman spectroscopy, topological material, Weyl semimetal

1 | INTRODUCTION

Weyl semimetals[1–8] have recently attracted much attention because of the unique physical phenomena they display due to their topological electronic band structures. Weyl semimetals host low-energy collective excitations behaving as massless Weyl fermions that emerge near the Weyl points in a three-dimensional momentum space, where the conduction and valence bands with linear dispersion touch.[1–3,9–11] Weyl points always exist as a pair with opposite chirality functioning as the source or sink of the Berry curvature flux field and behave in momentum space as a monopole or antimonopole of an effective magnetic field. A ternary ferromagnetic compound $Co_3Sn_2S_2$ has recently been identified as a magnetic topological semimetal that can host a Weyl semimetal phase using angle-resolved photoemission spectroscopy.[12,13] It has only three pairs of Weyl points arising from their broken time-reversal symmetry under preserved spatial inversion symmetry; the simple arrangement of the small number of type-I Weyl points provides an excellent platform for exploring Weyl fermion physics. $Co_3Sn_2S_2$ has been experimentally shown to exhibit a variety of intriguing physical properties and phenomena, including surface states with Fermi arc,[12–14] the anomalous Hall effect,[15–19] surface-localized one-dimensional chiral edge states,[20] Nernst effect,[21,22] exotic physical phenomena arising from their unique magnetism,[23–30] and efficient water oxidation.[31] Vacancy-modulated $Co_3Sn_2S_2$ was also proposed as an attractive candidate cathode material for aqueous Zn-ion batteries.[32] Thin films of $Co_3Sn_2S_2$ yet have a surface state reflecting Weyl features,[33,34] which may facilitate observation of a quantum anomalous Hall effect.[35] $Co_3Sn_2S_2$ has also been proposed as a promising candidate material to observe strong current-induced second harmonic generation.[36]

In contrast to the intensively studied electronic properties, as for Raman scattering of $Co_3Sn_2S_2$, experimental studies in the literature have still been limited. Although Raman spectra of $Co_3Sn_2S_2$-carbon nano onion composite[37] and $Co_3Sn_{1.8}S_2$ powders[32] have been reported, the fundamental Raman features of a single crystalline $Co_3Sn_2S_2$ have yet to be clarified experimentally. Here, we provide polarized Raman spectroscopy on a single crystal of $Co_3Sn_2S_2$. We observed two major Raman peaks of Γ point phonon modes showing different polarization dependence from each other, over continuous background emission signals that also showed clear polarization dependence. We assigned the symmetries of the two major phonon Raman modes based on the group theory and Raman tensor analyses. Moreover, we found that one of the two phonon Raman

peaks shows an asymmetric line-shape well fitted by the Breit–Wigner–Fano function, suggesting the Fano interference between the discrete phonon scattering and the continuous background; from this observation, the continuous background emission signals were attributed to electronic Raman scattering associated with low energy excitations near the Fermi energy, rather than hot luminescence or other extrinsic effects. The fundamental phonon and electronic Raman features of $Co_3Sn_2S_2$ clarified in this study are useful as a fingerprint for the quick experimental identification of the crystal structure. Moreover, the results suggest that Raman spectroscopy is an effective tool to study low energy electronic excitations and their interactions with phonons in $Co_3Sn_2S_2$.

2 | EXPERIMENTAL METHODS

According to a previous report, single crystals of $Co_3Sn_2S_2$ were grown by a self-flux method.[13] The raw material powders were mixed with a stoichiometric ratio of Co:Sn:S = 3:2:2, and the mixed powder placed in a quartz tube was heated to 1000°C over 48 h in a vacuum and held for 24 h. Then, the samples were cooled to 600°C for 168 h and held at 600°C for 24 h. The obtained sample included crystals of $Co_3Sn_2S_2$ with gray color. The crystals typically had a hexagonal shape with a flat surface as shown in Figure 1a. The typical thickness of the crystals ranged from several tens to 200 μm. The composition of the as-grown crystals was confirmed using energy-dispersive X-ray spectroscopy, and then the crystal structure was confirmed using X-ray diffraction (XRD) analysis. A single crystal was mounted with mineral oil on a MiTeGen MicroMounts and transferred to the kappa goniometer of an XRD spectrometer (RIGAKU XtaLAB Synergy-S system with 1.2-kW MicroMax-007HF microfocus rotating anode (Graphite-monochromated Mo Kα radiation [λ = 0.71073 Å]) and HyPix-6000HE hybrid photon-counting detector). Cell parameters were determined and refined, and raw frame data were integrated using CrysAlis[Pro] (Agilent Technologies, 2010). The structures were solved by direct methods with SHELXT[39] and refined using full-matrix least-squares techniques against F^2 (SHELXL-2018/3)[40] by using the Olex2 software package.[41] The intensities were corrected for Lorentz and polarization effects.

Unpolarized and polarized Raman spectroscopy was performed in the backscattering configuration using a commercial Raman microscope (inVia confocal Raman microscope; Renishaw, Wotton-under-Edge, UK) and a home-made optical setup, respectively. For unpolarized spectroscopy, the Raman signals were measured using a

FIGURE 1 (a) Microscope image of a typical single crystal of $Co_3Sn_2S_2$. (b) X-ray diffraction (XRD) pattern of a single crystal of $Co_3Sn_2S_2$. (c) The XRD data determine a unit cell of a single crystal of $Co_3Sn_2S_2$. Number of the Co, Sn, and S atoms within the volume outlined by the black lines indicating the unit cell boundary are counted as three, two, and two, respectively. (d) Crystal structure of $Co_3Sn_2S_2$ viewed along *c*-axis. Cristal structures are drawn using VESTA.[38] [Colour figure can be viewed at wileyonlinelibrary.com]
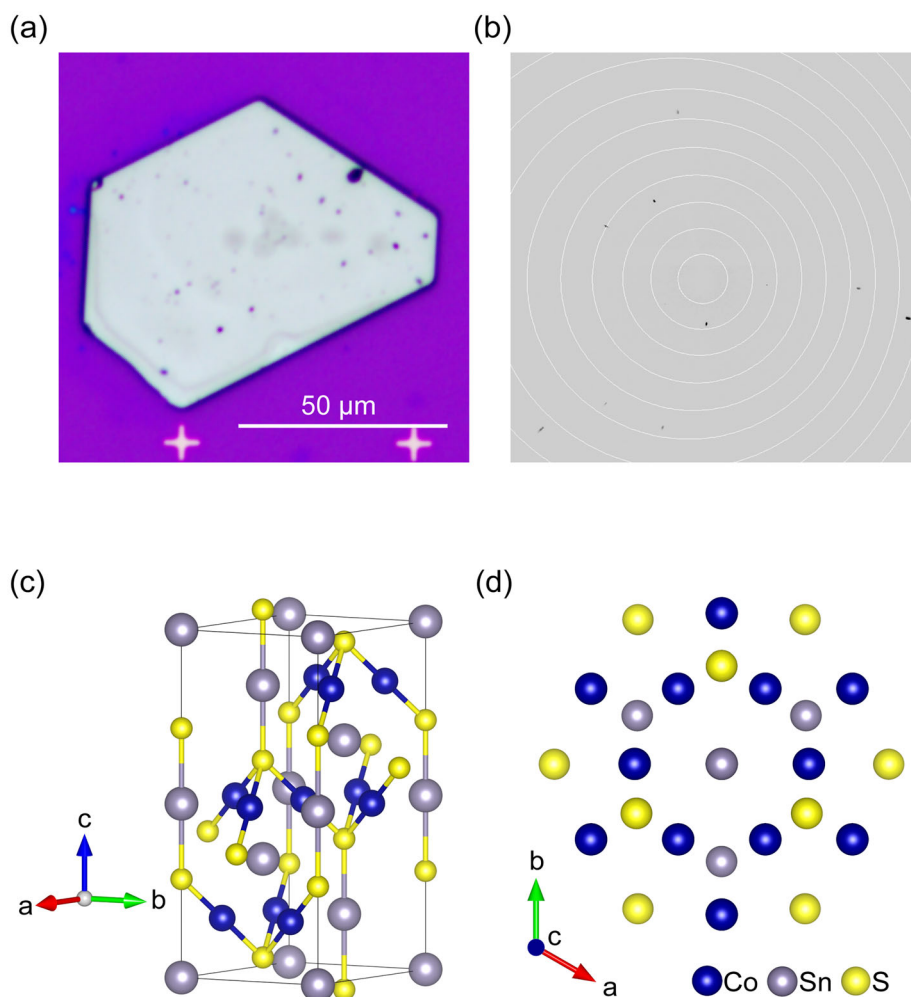

×100 objective lens with a numerical aperture (N.A.) of 0.9 under illumination of a 532-nm continuous-wave (CW) laser for the resonant excitation. The exposure time was set from 20 to 3600 s depending on the excitation laser power. For polarized Raman spectroscopy, a ×50 objective lens with N.A. = 0.42 was used for excitation and detection. The light source was a linear-polarized 532-nm CW laser with a power of 800 μW, which was within the linear response regime. The exposure time was 1200 s. The analyzer to resolve the polarization of the scattered photons was set behind an edge filter with a cutoff wavelength of 532-nm, and the scattered photons were detected using a spectrometer (Princeton Instruments, Acton SP2500) equipped with a nitrogen-cooled charged-coupled device camera (Princeton Instruments, Spec-10:400BReXII). The polarization-dependent detection sensitivity was corrected using unpolarized luminescent light. In polarized Raman spectroscopy, the sample was set on an automated sample rotation stage with a centering mechanism that allows the excitation of the identical spot on the single crystal for any sample rotation angles.

3 | RESULTS AND DISCUSSION

Figure 1b shows the XRD pattern of the single crystal, which shows some Bragg peaks reflecting each lattice plane. Figure 1c shows a schematic of the unit cell as determined using the results of XRD spectroscopy. The crystal structure has trigonal-trapezohedron symmetry of space-group $R\bar{3}m$ (No. 166) with the dihedral point group D_{3d}; it is composed of a Co_3Sn layer sandwiched between S and Sn atoms along the *c*-axis, and Co atoms form a Kagome network in each *a–b* plane (Figure 1d), which is consistent with the reported structure of $Co_3Sn_2S_2$ in the literature.[42]

Figure 2 shows a typical unpolarized Raman spectrum of a $Co_3Sn_2S_2$ single crystal with an excitation power of 27 μW in the range of 150–1130 cm^{-1}. Two sharp peaks were observed at 289 and 386 cm^{-1} over continuous background emission signals. These two peaks were also observed under 488-nm laser excitation (see Figure S1). The inset shows excitation power dependence of the wavenumbers of these two peak features. The redshifts of the peaks with increasing excitation power are
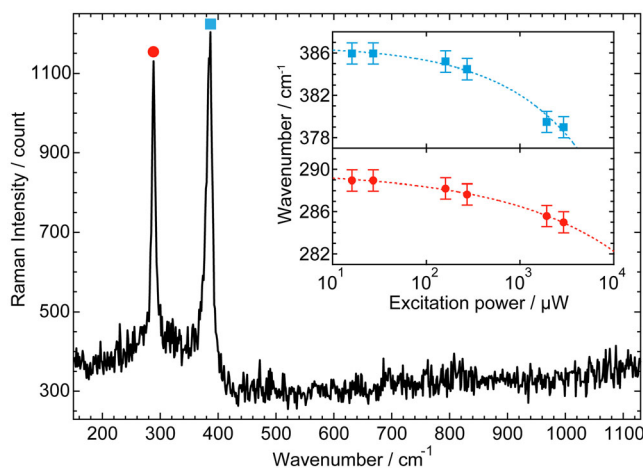
FIGURE 2 Raman scattering spectrum of a single crystal of $Co_3Sn_2S_2$. The excitation power, exposure time, and excitation spot size were 27 μW, 1800 s, and 1.0 μm, respectively. The spectrum was plotted after subtracting the equipment-derived background signals mainly owing to the thermal and electronic noise of the detection system. The inset shows excitation power dependence of the wavenumbers of the low-wavenumber peak (red circles) and the high-wavenumber peak (blue squares). The dotted curves are guides to the eye. [Colour figure can be viewed at wileyonlinelibrary.com]

presumably attributed to the softening of phonon modes due to increasing temperature or the modification in the Kohn anomaly effect[43–45] induced by the change in the electron occupancy near the Fermi energy characteristic in semimetals. We found that the wavenumbers were almost constant in the excitation power range below approximately 40 μW, as they indicate that the spectrum shown in Figure 2 was measured under weak excitation conditions where the laser-induced heating or other high-density effects were insignificant, and thus, the wavenumbers of 289 and 386 cm^{-1} can be regarded as the ones near room temperature.

The fundamental Raman-active phonon modes are optical at Γ point in the Brillouin zone. In the case of the $Co_3Sn_2S_2$ unit cell with the D_{3d} point group, the seven atoms per unit cell yield 21 phonon modes at the Γ point as $\Gamma_{vib} = A_{1g} + E_g + 6A_{2u} + 6E_u$, among which the Raman-active modes are non-degenerate A_{1g} and doubly-degenerated E_g modes, respectively (see Supporting Information S1 for the details of the symmetry analysis). These Raman-active modes could exhibit two one-phonon Raman peaks, consistent with the experimental observation shown in Figure 2. To further assign the symmetries of the two observed modes, we can use the fact that these Raman peaks should show different polarization dependence, owing to the difference in the Raman tensors R for these phonon modes[46] in the forms,

$$R(A_{1g}) = \begin{pmatrix} a & 0 & 0 \\ 0 & a & 0 \\ 0 & 0 & b \end{pmatrix},$$

$$R(E_g) = \begin{pmatrix} c & 0 & 0 \\ 0 & -c & d \\ 0 & d & 0 \end{pmatrix}, \begin{pmatrix} 0 & -c & -d \\ -c & 0 & 0 \\ -d & 0 & 0 \end{pmatrix}, \quad (1)$$

where a, b, c, d are constants. The Raman scattering intensity (I_{Raman}) is proportional to the product of R for each mode with the incident ($\mathbf{e}_i$) and scattered ($\mathbf{e}_s$) photon polarization vectors as

$$I_{Raman} \propto |\mathbf{e}_i \cdot R \cdot \mathbf{e}_s|^2. \quad (2)$$

We are using Equations (1) and (2), the polarization dependence of each mode can be predicted.

Let us now set the experimental coordinate so that the incident light travels along the z-axis coincident with the c-axis of the crystal, as shown in Figure 3a. Then the polarization vectors are expressed as $\mathbf{e}_i = (\cos\theta_i, \sin\theta_i, 0)$ and $\mathbf{e}_s = (\cos\theta_s, \sin\theta_s, 0)$, where θ_i and θ_s are the azimuthal angles of the incident and scattered polarizations, respectively. When $\theta_i = \theta_s$ (hereafter, referred to as VV, which corresponds to $Z(XX)\overline{Z}$ configuration in Porto's notation when $\theta_i = \theta_s = 0$), Equations (1) and (2) immediately results in $I_{Raman}^{VV}(A_{1g}) \propto a^2$, which is independent of the sample rotation angle $\theta (= \theta_i)$ around the c-axis. With regard to the E_g modes, the net Raman intensity is obtained as a sum of the responses of the two degenerate modes as $I_{Raman}^{VV}(E_g) \propto c^2(\cos^2 2\theta + \sin^2 2\theta) = c^2$, which is also independent of θ. Thus, for the VV configuration, both A_{1g} and E_g peaks can exhibit finite Raman scattering intensity and are predicted to show Raman scattering independently of the crystal angle θ. In contrast, when $\mathbf{e}_i \perp \mathbf{e}_s$, namely, $\theta_s = \theta_i \pm \pi/2$ (hereafter, referred to as VH, which corresponds to $Z(XY)\overline{Z}$ configuration in Porto's notation when $\theta_s = 0$ and $\theta_i \pm \pi/2$), the responses of the A_{1g} and E_g modes show a distinctive difference; $I_{Raman}^{VH}(A_{1g}) = 0$ and $I_{Raman}^{VH}(E_g) \propto c^2$ are obtained using Equations (1) and (2). Therefore, the responses for the VH configuration should show only the E_g mode peak with no sample angle dependence, which is the critical difference to be used to distinguish the Raman peaks of the A_{1g} and E_g modes.

According to the above predictions, we performed polarized Raman spectroscopy under the VV and VH configurations as shown in Figure 3a to assign the phonon symmetries corresponding to the observed Raman peaks. For the VV and VH measurements, the orientation of the analyzer was set parallel and perpendicular to the

—WILEY

(a)

(b)
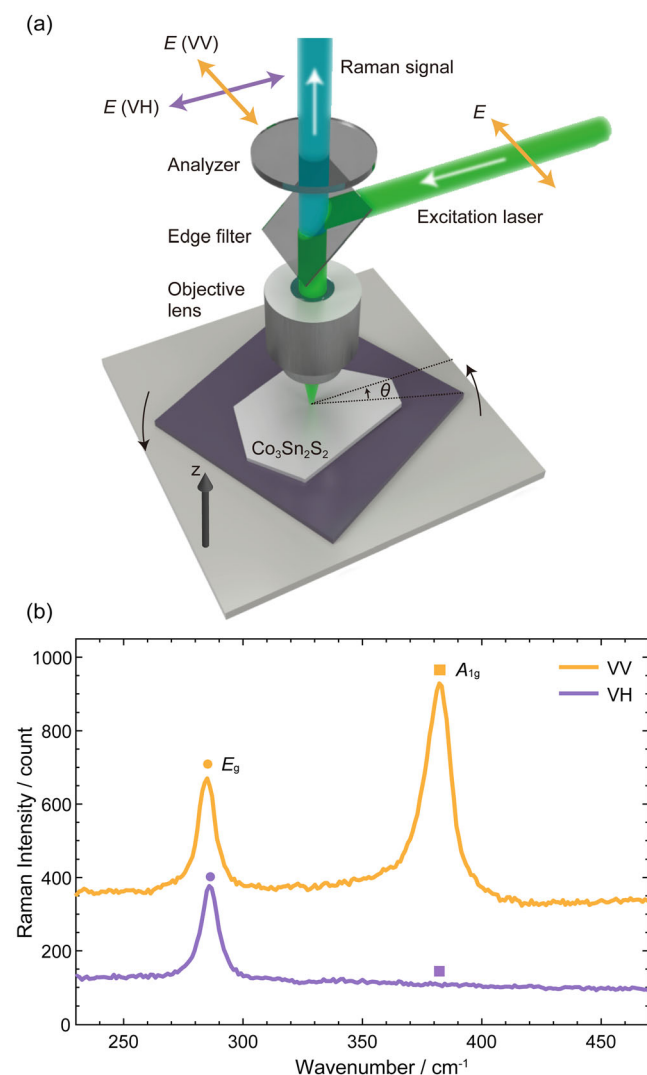
FIGURE 3 (a) Schematic of an optical setup for polarization-resolved Raman spectroscopy. The orange and purple arrows indicate the polarization direction of the electric field (E). θ is the rotation angle of the sample. The tilt of the edge filter to the detection optical path is drawn steeply for clarity (the filter was tilted 11° to the objective lens in the actual configuration). (b) Polarization-resolved Raman spectra of co-polarization (VV; orange) and cross-polarization (VH; purple) configurations. The spectra were plotted after subtracting the equipment-derived background signals mainly owing to the thermal and electronic noise of the detection system. [Colour figure can be viewed at wileyonlinelibrary.com]

incident light polarization, respectively. Figure 3b compares typical Raman spectra in the VV and VH configurations. Only the low-wavenumber peak was observed in the VH configuration, while both the low- and high-wavenumber peaks were observed in the VV configuration. In addition, the continuous background signal intensity also depended on the detection configuration;

the intensity for the VV configuration was much higher than that in the VH configuration.

The Raman spectra in VV and VH configurations were also measured while rotating the sample with a rotation step of 10°. As shown in Figure 4, intensities of the two peaks (a–d) and the continuous background signals (e) showed no-rotation-angle dependence; these results confirm that the missing of the high-wavenumber peak for the VH configuration is not due to the sample angle dependence but surely originates from the difference in the response under the VV and VH configurations as predicted by the group theory and Raman tensor analysis. By comparing these observations with the prediction of the missing A_{1g} mode peak only for the VH configuration, the low- ($289\,cm^{-1}$) and high-wavenumber ($386\,cm^{-1}$) peaks are unambiguously attributed to E_g and A_{1g} phonon modes, respectively. With regard to the absolute values of these phonon energies, Xu et al.[47] recently reported the phonon dispersion relation in $Co_3Sn_2S_2$ based on ab-initio calculation and doubly degenerate modes at approximately 35–40 meV and non-degenerate modes at approximately 45–50 meV were found at the Γ point. On the other hand, the experimental results in this study showed degenerate E_g mode at $289\,cm^{-1}$ ($\sim$36 meV) and non-degenerate A_{1g} phonon mode at $386\,cm^{-1}$ ($\sim$48 meV). Therefore, the observed phonon energies are consistent with the theoretically predicted ones in $Co_3Sn_2S_2$ at the Γ point.

For further analysis, we examined the spectral line-shapes of the E_g and A_{1g} peaks as shown in left panels in Figure 4a–c. We found that only the A_{1g} peak has asymmetric line-shape that can be well described by the Breit–Wiger–Fano (BWF) function.[48–51]

$$I(\omega) = I_0 \frac{\left(1 + \frac{s(\omega)}{q}\right)^2}{1 + s(\omega)^2}, \qquad (3)$$

where $s(\omega) = (\omega - \omega_0)/\Gamma$. By fitting procedure, we obtained the values of the constant $q = -7.91$ for the A_{1g} mode and $q = 548$ for the E_g mode, respectively. As the absolute value of $1/q$ corresponds to the degree of asymmetry, the low-wavenumber E_g mode with $1/q < 0.002$ is almost symmetric and could be well fitted using a symmetric Lorentzian function. The BWF line-shape of the A_{1g} mode suggests that there exists the Fano interference[52] between the A_{1g} phonon scattering and the continuous background component showing the similar polarization dependence to the A_{1g} phonon Raman scattering. These results suggest that the origin of the polarization-dependent continuous background could be intrinsic electronic Raman scattering associated with the low energy electronic excitation near the Fermi energy,
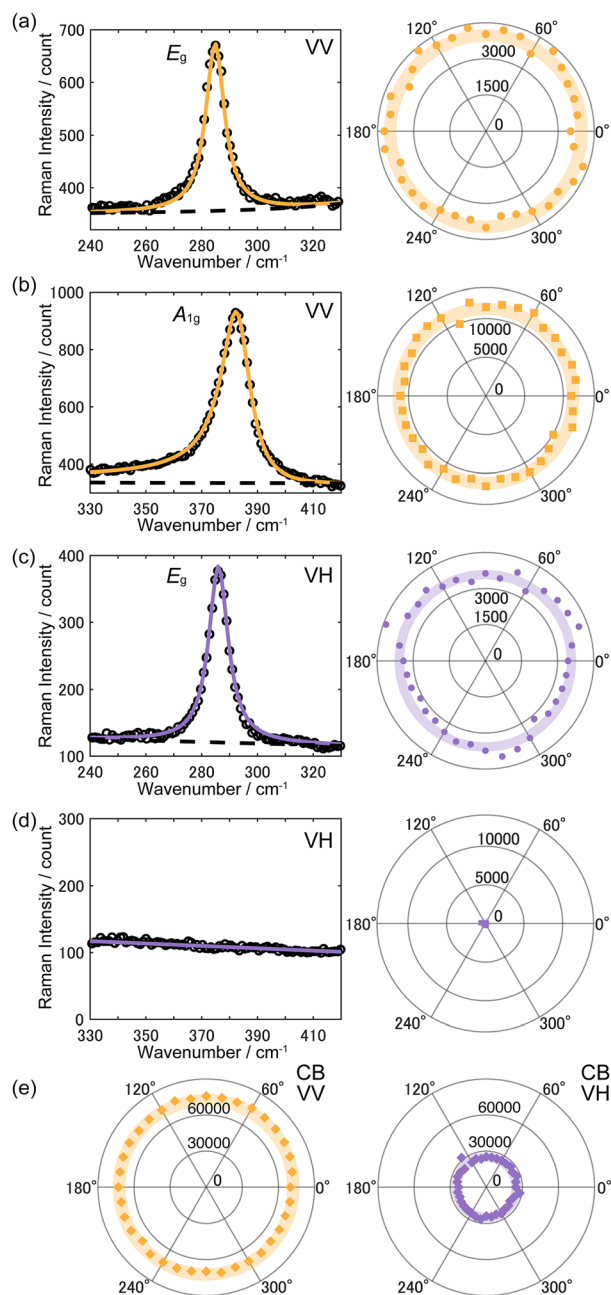
FIGURE 4 Peak fitting analyses of the polarization resolved Raman spectra. (a) E_g peak in VV configuration, (b) A_{1g} peak in VV configuration, (c) E_g peak in VH configuration, (d) no peak in VH configuration and (e) constant background (CB) intensities in VV (left) and VH (right) configurations. Left panels in (a–d) show the measured spectra (black open circles) and fit results (solid curves), and right panels indicate integrated intensity of each feature as a function of the crystal rotation angle. Data integrated for all the angles are plotted in the left panels of (a–d). The values of the constants in Equation (3) were obtained as $\omega_0 = 383$ (cm^{-1}), $q = -7.91$, $\Gamma = 6.26$ (cm^{-1}) for the A_{1g} mode and $\omega_0 = 285$ (cm^{-1}), $q = 548$, $\Gamma = 4.16$ (cm^{-1}) for the E_g mode, respectively. Background intensities plotted in (e) were evaluated as integrated intensities in the wavenumber range between 240 and 450 cm^{-1} after subtracting the contribution from the peak features. [Colour figure can be viewed at wileyonlinelibrary.com]

rather than hot luminescence or other extrinsic effects such as incoherent luminescence from the surface impurities or oxides.

4 | CONCLUSION

In summary, we studied Raman scattering of $Co_3Sn_2S_2$, which has attracted growing attention as a magnetic topological semimetal, via unpolarized and polarized Raman spectroscopy. We found that the single crystal of $Co_3Sn_2S_2$, of which the XRD measurements guaranteed the crystal structure, shows two major Raman scattering peaks of Raman-active Γ point phonon modes at 289 cm^{-1} and 386 cm^{-1}, together with a continuous background emission signal. The polarization- and rotation-angle-resolved Raman spectroscopy revealed a distinctive difference in the responses for the collinear VV and the cross-polarized VH Raman scattering responses for both of the phonon Raman peaks and the continuous background. Simultaneously, no rotation-angle dependence was observed for both configurations. By comparing the observations to the predictions from the group theory and Raman tensor analysis, the low- and high-wavenumber Raman peaks were unambiguously attributed to E_g and A_{1g} phonon modes, respectively. Furthermore, it was revealed that only the A_{1g} phonon mode peak shows asymmetric line shape that can be well fitted by the BWF function. These results suggest that the Fano interference of the A_{1g} phonon Raman scattering with the continuous electronic Raman background associated with the low energy electronic excitation near the Fermi energy. The fundamental information of the Raman fingerprint of $Co_3Sn_2S_2$ obtained in this study is helpful for quick experimental assessment of the crystal structure and verification of theoretical calculations by comparing simulated phonon energies with the experimental counterparts. Moreover, the findings shed light on the importance of Raman spectroscopy as an effective tool to probe low energy electronic excitations and their interactions with phonons in $Co_3Sn_2S_2$.

DATA AVAILABILITY STATEMENT

Data available on request from the authors

ORCID

Taishi Nishihara https://orcid.org/0000-0001-6973-2005

Yasutomo Segawa https://orcid.org/0000-0001-6439-8546

Yuhei Miyauchi https://orcid.org/0000-0002-0945-0265

REFERENCES

[1] X. Wan, A. M. Turner, A. Vishwanath, S. Y. Savrasov, *Phys. Rev. B* **2011**, *83*, 205101.

[2] A. A. Burkov, L. Balents, *Phys. Rev. Lett.* **2011**, *107*, 127205.

[3] S. M. Young, S. Zaheer, J. C. Y. Teo, C. L. Kane, E. J. Mele, A. M. Rappe, *Phys. Rev. Lett.* **2012**, *108*, 140405.

[4] B. Yan, C. Felser, *Annu. Rev. Condens. Matter Phys.* **2017**, *8*, 337.

[5] N. P. Armitage, E. J. Mele, A. Vishwanath, *Rev. Mod. Phys.* **2018**, *90*, 15001.

[6] N. Nagaosa, T. Morimoto, Y. Tokura, *Nat. Rev. Mater.* **2020**, *5*, 621.

[7] C. Zhang, Y. Zhang, H.-Z. Lu, X. C. Xie, F. Xiu, *Nat. Rev. Phys.* **2021**, *3*, 660.

[8] H. W. Liu, P. Richard, Z. D. Song, L. X. Zhao, Z. Fang, G.-F. Chen, H. Ding, *Phys. Rev. B* **2015**, *92*, 064302.

[9] S.-Y. Xu, I. Belopolski, N. Alidoust, M. Neupane, G. Bian, C. Zhang, R. Sankar, G. Chang, Z. Yuan, C.-C. Lee, S.-M. Huang, H. Zheng, J. Ma, D. S. Sanchez, B. Wang, A. Bansil, F. Chou, P. P. Shibayev, H. Lin, S. Jia, M. Z. Hasan, *Science* **2015**, *349*, 613.

[10] S.-Y. Xu, N. Alidoust, I. Belopolski, Z. Yuan, G. Bian, T.-R. Chang, H. Zheng, V. N. Strocov, D. S. Sanchez, G. Chang, C. Zhang, D. Mou, Y. Wu, L. Huang, C.-C. Lee, S.-M. Huang, B. Wang, A. Bansil, H.-T. Jeng, T. Neupert, A. Kaminski, H. Lin, S. Jia, M. Z. Hasan, *Nat. Phys.* **2015**, *11*, 748.

[11] B. Q. Lv, H. M. Weng, B. B. Fu, X. P. Wang, H. Miao, J. Ma, P. Richard, X. C. Huang, L. X. Zhao, G. F. Chen, Z. Fang, X. Dai, T. Qian, H. Ding, *Phys. Rev. X* **2015**, *5*, 031013.

[12] D. F. Liu, A. J. Liang, E. K. Liu, Q. N. Xu, Y. W. Li, C. Chen, D. Pei, W. J. Shi, S. K. Mo, P. Dudin, T. Kim, C. Cacho, G. Li, Y. Sun, L. X. Yang, Z. K. Liu, S. S. P. Parkin, C. Felser, Y. L. Chen, *Science* **2019**, *365*, 1282.

[13] N. Morali, R. Batabyal, P. K. Nag, E. Liu, Q. Xu, Y. Sun, B. Yan, C. Felser, N. Avraham, H. Beidenkopf, *Science* **2019**, *365*, 1286.

[14] Q. Xu, E. Liu, W. Shi, L. Muechler, J. Gayles, C. Felser, Y. Sun, *Phys. Rev. B* **2018**, *97*, 235416.

[15] E. Liu, Y. Sun, N. Kumar, L. Muechler, A. Sun, L. Jiao, S.-Y. Yang, D. Liu, A. Liang, Q. Xu, J. Kroder, V. Süß, H. Borrmann, C. Shekhar, Z. Wang, C. Xi, W. Wang, W. Schnelle, S. Wirth, Y. Chen, S. T. B. Goennenwein, C. Felser, *Nat. Phys.* **2018**, *14*, 1125.

[16] Q. Wang, Y. Xu, R. Lou, Z. Liu, M. Li, Y. Huang, D. Shen, H. Weng, S. Wang, H. Lei, *Nat. Commun.* **2018**, *9*, 3681.

[17] J. Shen, Q. Zeng, S. Zhang, H. Sun, Q. Yao, X. Xi, W. Wang, G. Wu, B. Shen, Q. Liu, E. Liu, *Adv. Funct. Mater.* **2020**, *30*, 2000830.

[18] J. Shen, Q. Yao, Q. Zeng, H. Sun, X. Xi, G. Wu, W. Wang, B. Shen, Q. Liu, E. Liu, *Phys. Rev. Lett.* **2020**, *125*, 086602.

[19] Z. Guguchia, J. A. T. Verezhak, D. J. Gawryluk, S. S. Tsirkin, J.-X. Yin, I. Belopolski, H. Zhou, G. Simutis, S-S. Zhang, T. A. Cochran, G. Chang, E. Pomjakushina, L. Keller, Z. Skrzeczkowska, Q. Wang, H. C. Lei, R. Khasanov, A. Amato, S. Jia, T. Neupert, H. Luetkens, M. Z. Hasan, *Nat. Commun.* **2020**, *11*, 559.

[20] S. Howard, L. Jiao, Z. Wang, N. Morali, R. Batabyal, P. Kumar-Nag, N. Avraham, H. Beidenkopf, E. Liu, C. Shekhar, C. Felser, T. Hughes, V. Madhavan, *Nat. Commun.* **2021**, *12*, 4269.

[21] S. N. Guin, P. Vir, Y. Zhang, N. Kumar, S. J. Watzman, C. Fu, E. Liu, K. Manna, W. Schnelle, J. Gooth, C. Shekhar, Y. Sun, C. Felser, *Adv. Mater.* **2019**, *31*, 1806622.

[22] H. Yang, W. You, J. Wang, J. Huang, C. Xi, X. Xu, C. Cao, M. Tian, Z.-A. Xu, J. Dai, Y. Li, *Phys. Rev. Mater.* **2020**, *4*, 024202.

[23] M. A. Kassem, Y. Tabata, T. Waki, H. Nakamura, *Phys. Rev. B* **2017**, *96*, 014429.

[24] J.-X. Yin, S. S. Zhang, G. Chang, Q. Wang, S. S. Tsirkin, Z. Guguchia, B. Lian, H. Zhou, K. Jiang, I. Belopolski, N. Shumiya, D. Multer, M. Litskevich, T. A. Cochran, H. Lin, Z. Wang, T. Neupert, S. Jia, H. Lei, M. Z. Hasan, *Nat. Phys.* **2019**, *15*, 443.

[25] Y. Xing, J. Shen, H. Chen, L. Huang, Y. Gao, Q. Zheng, Y.-Y. Zhang, G. Li, B. Hu, G. Qian, L. Cao, X. Zhang, P. Fan, R. Ma, Q. Wang, Q. Yin, H. Lei, W. Ji, S. Du, H. Yang, W. Wang, C. Shen, X. Lin, E. Liu, B. Shen, Z. Wang, H.-J. Gao, *Nat. Commun.* **2020**, *11*, 5613.

[26] S. Howlader, S. Saha, R. Kumar, V. Nagpal, S. Patnaik, T. Das, G. Sheet, *Phys. Rev. B* **2020**, *102*, 104434.

[27] R. Yang, T. Zhang, L. Zhou, Y. Dai, Z. Liao, H. Weng, X. Qiu, *Phys. Rev. Lett.* **2020**, *124*, 077403.

[28] Q. Zhang, S. Okamoto, G. D. Samolyuk, M. B. Stone, A. I. Kolesnikov, R. Xue, J. Yan, M. A. McGuire, D. Mandrus, D. A. Tennant, *Phys. Rev. Lett.* **2021**, *127*, 117201.

[29] Y. Okamura, S. Minami, Y. Kato, Y. Fujishiro, Y. Kaneko, J. Ikeda, J. Muramoto, R. Kaneko, K. Ueda, V. Kocsis, N. Kanazawa, Y. Taguchi, T. Koretsune, K. Fujiwara, A. Tsukazaki, R. Arita, Y. Tokura, Y. Takahashi, *Nat. Commun.* **2020**, *11*, 4619.

[30] I. Belopolski, T. A. Cochran, X. Liu, Z.-J. Cheng, X. P. Yang, Z. Guguchia, S. S. Tsirkin, J.-X. Yin, P. Vir, G. S. Thakur, S. S. Zhang, J. Zhang, K. Kaznatcheev, G. Cheng, G. Chang, D. Multer, N. Shumiya, M. Litskevich, E. Vescovo, T. K. Kim, C. Cacho, N. Yao, C. Felser, T. Neupert, M. Z. Hasan, *Phys. Rev. Lett.* **2021**, *127*, 256403.

[31] G. Li, Q. Xu, W. Shi, C. Fu, L. Jiao, M. E. Kamminga, M. Yu, H. Tüysüz, N. Kumar, V. Süß, R. Saha, A. K. Srivastava, S. Wirth, G. Auffermann, J. Gooth, S. Parkin, Y. Sun, E. Liu, C. Felser, *Sci. Adv.* **2019**, *5*, eaaw9867.

[32] Y. Zhao, Y. Zhu, F. Jiang, Y. Li, Y. Meng, Y. Guo, Q. Li, Z. Huang, S. Zhang, R. Zhang, J. C. Ho, Q. Zhang, W. Liu, C. Zhi, *Angew. Chemie Int. Ed.* **2022**, *61*, e202111826.

[33] J. Ikeda, K. Fujiwara, J. Shiogai, T. Seki, K. Nomura, K. Takanashi, A. Tsukazaki, *Commun. Phys.* **2021**, *4*, 117.

[34] J. Ikeda, K. Fujiwara, J. Shiogai, T. Seki, K. Nomura, K. Takanashi, A. Tsukazaki, *Commun. Mater.* **2021**, *2*, 18.

[35] L. Muechler, E. Liu, J. Gayles, Q. Xu, C. Felser, Y. Sun, *Phys. Rev. B* **2020**, *101*, 115106.

[36] K. Takasan, T. Morimoto, J. Orenstein, J. E. Moore, *Phys. Rev. B* **2021**, *104*, L161202.

[37] W. Cheng, B. Wan, J. Shen, H. Tang, S. Xü, G. Wang, E. Liu, H. Gou, *Chem. Eng. J.* **2022**, *443*, 136420.

[38] K. Momma, F. Izumi, *J. Appl. Crystallogr.* **2011**, *44*, 1272.

[39] G. M. Sheldrick, *Acta Crystallogr. Sect. A Found. Adv.* **2015**, *71*, 3.

[40] G. M. Sheldrick, *Struct. Chem.* **2015**, *71*, 3.

[41] O. V. Dolomanov, L. J. Bourhis, R. J. Gildea, J. A. K. Howard, H. Puschmann, *J. Appl. Crystallogr.* **2009**, *42*, 339.

[42] A. Umetani, E. Nagoshi, T. Kubodera, M. Matoba, *Physica B Condens. Matter* **2008**, *403*, 1356.

[43] W. Kohn, *Phys. Rev. Lett.* **1959**, *2*, 393.

[44] E. H. Hasdeo, A. R. T. Nugraha, M. S. Dresselhaus, R. Saito, *Phys. Rev. B* **2016**, *94*, 075104.

[45] T. Nguyen, F. Han, N. Andrejevic, R. Pablo-Pedro, A. Apte, Y. Tsurimaki, Z. Ding, K. Zhang, A. Alatas, E. E. Alp, S. Chi, J. Fernandez-Baca, M. Matsuda, D. A. Tennant, Y. Zhao, Z. Xu, J. W. Lynn, S. Huang, M. Li, *Phys. Rev. Lett.* **2020**, *124*, 236401.

[46] D. Tuschel, *Spectroscopy* **2020**, *35*, 5.

[47] Y. Xu, J. Zhao, C. Yi, Q. Wang, Q. Yin, Y. Wang, X. Hu, L. Wang, E. Liu, G. Xu, L. Lu, A. A. Soluyanov, H. Lei, Y. Shi, J. Luo, Z.-G. G. Chen, *Nat. Commun.* **2020**, *11*, 3985.

[48] M. V. Klein, in *Electronic Raman scattering, in light scattering in solids*, (Ed: M. Cardona), Springer, Berlin **1975**.

[49] P. C. Eklund, K. R. Subbaswamy, *Phys. Rev. B* **1979**, *20*, 5157.

[50] D. Yoon, D. Jeong, H. J. Lee, R. Saito, Y. W. Son, H. C. Lee, H. Cheong, *Carbon N. Y.* **2013**, *61*, 373.

[51] E. H. Hasdeo, A. R. T. Nugraha, M. S. Dresselhaus, R. Saito, *Phys. Rev. B* **2014**, *90*, 245140.

[52] U. Fano, *Phys. Rev.* **1866**, *1961*, 124.

SUPPORTING INFORMATION

Additional supporting information can be found online in the Supporting Information section at the end of this article.